



# CHORUS

This is the accepted manuscript made available via CHORUS. The article has been published as:

## Probing antiferromagnetic coupling in magnetic insulator/metal heterostructures

Patrick Quarterman, Yabin Fan, Zhijie Chen, Christopher J. Jensen, Rajesh V. Chopdekar, Dustin A. Gilbert, Megan E. Holtz, Mark D. Stiles, Julie A. Borchers, Kai Liu, Luqiao Liu, and Alexander J. Grutter

Phys. Rev. Materials **6**, 094418 — Published 30 September 2022

DOI: [10.1103/PhysRevMaterials.6.094418](https://doi.org/10.1103/PhysRevMaterials.6.094418)

# 1 PROBING ANTIFERROMAGNETIC COUPLING IN MAGNETIC 2 INSULATOR/METAL HETEROSTRUCTURES

3 **Authors:** P. Quarterman<sup>1\*</sup>, Yabin Fan<sup>2</sup>, Zhijie Chen<sup>3</sup>, Christopher J. Jensen<sup>3</sup>, Rajesh V.  
4 Chopdekar<sup>4</sup>, Dustin A. Gilbert<sup>5</sup>, Megan E. Holtz<sup>6,7</sup>, Mark D. Stiles<sup>8</sup>, Julie A. Borchers<sup>1</sup>, Kai Liu<sup>3</sup>,  
5 Luqiao Liu<sup>2</sup>, and Alexander J. Grutter<sup>1\*</sup>

## 6 **Affiliations:**

7 <sup>1</sup>*NIST Center for Neutron Research, National Institute of Standards and Technology, 100 Bureau  
8 Dr., Gaithersburg, Maryland 20899, USA*

9 <sup>2</sup>*Microsystems Technology Laboratories, Massachusetts Institute of Technology, Cambridge,  
10 Massachusetts 02139, USA*

11 <sup>3</sup>*Physics Department, Georgetown University, Washington, D.C. 20057, United States*

12 <sup>4</sup>*Advanced Light Source, Lawrence Berkeley National Laboratory, Berkeley, California 94720,  
13 USA*

14 <sup>5</sup>*Department of Materials Science and Engineering, University of Tennessee, Knoxville, Tennessee  
15 37996, USA*

16 <sup>6</sup>*Materials Measurement Laboratory, National Institute of Standards and Technology, 100 Bureau  
17 Dr. Gaithersburg, Maryland 20899, USA*

18 <sup>7</sup>*Department of Metallurgical and Materials Engineering, Colorado School of Mines, Golden, CO  
19 80401, USA*

20 <sup>8</sup>*Center for Nanoscale Science and Technology, National Institute of Standards and Technology,  
21 100 Bureau Dr. Gaithersburg, Maryland 20899, USA*

22 \*To whom correspondence should be addressed. Email: patrick.quarterman@nist.gov,  
23 alexander.grutter@nist.gov

## 24 25 **ABSTRACT:**

26 Using depth and element resolved characterization, we report insights into  
27 antiferromagnetic coupling in Y<sub>3</sub>Fe<sub>5</sub>O<sub>12</sub>/permalloy (YIG/Py) and Y<sub>3</sub>Fe<sub>5</sub>O<sub>12</sub>/Co (YIG/Co) thin film  
28 heterostructures grown on Si/SiO<sub>2</sub> and Gd<sub>3</sub>Ga<sub>5</sub>O<sub>12</sub> substrates. We build on recent work  
29 demonstrating antiferromagnetic coupling in polycrystalline YIG/metallic-ferromagnetic systems  
30 by characterizing differences in the structural and magnetic properties which depend on the choice  
31 of ferromagnet (Py vs. Co), seed layer (with and without Pt), and substrate (Si/SiO<sub>2</sub> vs.  
32 Gd<sub>3</sub>Ga<sub>5</sub>O<sub>12</sub>). These differences in the sample structure manifest as notable changes in interface

33 coupling sign, magnetic reversal mechanisms, magnetic depth profiles, and domain structure.  
34 Through a combination of magnetometry, polarized neutron reflectometry, and X-ray  
35 photoemission electron microscopy, a comprehensive picture of the magnetic interactions is  
36 realized, with lateral- and depth-resolution at sub-micrometer and nanometer scales, respectively.  
37 These results confirm that both Co and Py share a preference to align antiparallel to polycrystalline  
38 YIG grown on some substrates (Si/SiO<sub>2</sub> and Si/SiO<sub>2</sub>/Pt), while coupling ferromagnetically with  
39 highly oriented YIG on (111) Gd<sub>3</sub>Ga<sub>5</sub>O<sub>12</sub> and (110) Gd<sub>3</sub>Ga<sub>5</sub>O<sub>12</sub>/Pt substrates. The complex  
40 interplay among magnetic interactions at the YIG/FM interface has important implications for  
41 spintronic and magnonic devices based on this platform.

42

## 43 I. INTRODUCTION

44

45 Heterostructures consisting of magnetic insulators and ferromagnetic metals are of wide  
46 interest as platforms for magnon physics and applications in non-volatile memories [1]. Yttrium-  
47 iron-garnet ( $\text{Y}_3\text{Fe}_5\text{O}_{12}$ , YIG) is an extensively studied ferrimagnetic insulator with a low Gilbert  
48 damping constant [2] and long spin-wave propagation lifetime [3,4], which make it an important  
49 candidate for use in domain wall memories [5] and magnon spintronics [6,7]. In the context of  
50 magnon studies, YIG is capable of hosting standing spin waves (SSW) and interlayer magnon-  
51 magnon coupling when in proximity to a soft ferromagnetic metal [8–10]. YIG-based spin wave  
52 structures are also exciting for enabling quantum functionalities [11–13]. The interlayer exchange  
53 interaction in YIG/metal ferromagnetic (FM) systems has been demonstrated to exhibit the  
54 magnon spin-valve effect [14,15]. Magnon spin-valves are potentially advantageous compared to  
55 traditional magnetic memories, as transmitting information through pure spin currents rather than  
56 a spin-polarized current dramatically reduces the associated Joule heating, improving their energy  
57 efficiency [6].

58 YIG films used for fundamental research are typically grown epitaxially on  $\text{Gd}_3\text{Ga}_5\text{O}_{12}$   
59 (GGG) substrates. However, GGG is not compatible with CMOS-based heterostructures, limiting  
60 the technological relevance of these systems. In addition, there have been numerous reports of  
61 interdiffusion between YIG thin films and GGG substrates, leading to complex magnetic  
62 interactions which vary from sample to sample and degrade device performance [16,17]. While  
63 the development of YIG/FM hybrid structures on Si/SiO<sub>2</sub> substrates would yield significant  
64 advantages, the exploration of such systems remains in its infancy and much of the associated  
65 materials physics is poorly understood. For example, we have recently reported intrinsic  
66 antiparallel coupling in sputtered Si/SiO<sub>2</sub>/Pt/YIG/permalloy ( $\text{Ni}_{80}\text{Fe}_{20}$ , Py) heterostructures with a

67 coupling field as large as 150 mT [18]. That work demonstrated that the coupling is due to an  
68 interfacial exchange interaction rather than dipole interactions, and that the magnetization reversal  
69 process can be tuned by changing the ratio of the YIG and Py magnetic moments through their  
70 respective layer thicknesses. Furthermore, we have used the antiparallel coupling in this Si-based  
71 heterostructure to fabricate a magnon spin valve with an ON/OFF ratio of 130% at room  
72 temperature. However, much remains unknown about this unexpected magnetic configuration,  
73 particularly the underlying source of this antiparallel exchange interaction and its applicability to  
74 other FM layers or substrates.

75 Here we note the work of S. Klingler *et al.* which suggested a comparable magnetic  
76 configuration in a YIG/Co heterostructure with a very different geometry [8]. In that study, the  
77 authors interrogated specially prepared 1  $\mu\text{m}$  YIG films grown on (111)-oriented GGG substrates  
78 by liquid phase epitaxy and capped with 35 nm to 50 nm of Co, proposing an antiparallel  
79 configuration with a vertical domain wall in the YIG layer. The YIG surface in S. Klingler *et al.*  
80 was prepared through etching and *in-situ* annealing prior to Co deposition.

81 When considered in tandem, these observations of antiparallel alignment of YIG and FM  
82 [8, 18] suggest that the interface coupling is determined by a complex interplay among a number  
83 of factors. For example, surface termination and interface chemistry may play a critical role,  
84 depending on whether the dominant coupling mechanism is direct exchange or oxygen-mediated  
85 superexchange between Fe in the YIG and Fe/Co/Ni in the adjacent metal. If the interfacial metal  
86 forms surface bonds with YIG oxygen, the sign of the resulting exchange will depend on unknown  
87 ferromagnetic metal valence states at the surface as well as bond angles across the interface, all of  
88 which vary with surface termination. It may therefore be expected that  $\text{Fe}^{2+} - \text{O} - \text{Fe}$  superexchange  
89 may yield a different exchange coupling sign than, for example,  $\text{Fe}^{3+} - \text{O} - \text{Co}$  superexchange or

90  $\text{Fe}^{2+}$  - Ni direct exchange. Magnetic disorder and frustration at a polycrystalline YIG surface may  
91 also play a role. Lastly, we note that the growth of iron garnet systems is a notoriously  
92 temperamental process, and any unexpected outcomes such as antiparallel coupling must be  
93 carefully assessed to ensure they do not arise from sample quality issues induced by a specific  
94 growth process such as the dc magnetron sputtering used in reference 18. [18]

95         Unfortunately, the complexity of a polycrystalline metal-oxide interface with multiple  
96 valence states and an unknown surface termination renders the origin of antiparallel interface  
97 coupling at YIG/FM interfaces impossible to determine theoretically. Instead, we provide  
98 additional insight experimentally using a suite of characterization techniques including polarized  
99 neutron reflectometry (PNR), X-ray photoemission electron microscopy (XPEEM),  
100 magnetometry, and X-ray diffraction (XRD). These techniques are applied to a range of  
101 heterostructures including YIG/Py grown on Si/SiO<sub>2</sub> with and without a Pt seed layer, YIG/Py  
102 grown on (111) GGG and (110) GGG/Pt, and YIG/Co grown on Si/SiO<sub>2</sub>/Pt. This selection of  
103 samples allows for variation in ferromagnetic metal selection, film quality, crystallographic  
104 orientation, and surface termination. These results yield critical insights for the design and  
105 implementation of CMOS-compatible magnetic insulator/ferromagnetic metal hybrid structures  
106 for magnon logic.

## 107 108 **II. METHODS**

109  
110         On (001)-oriented Si/SiO<sub>2</sub> substrates, we studied a series of thin film samples with nominal  
111 stack structures of Pt (0 nm or 10 nm)/YIG (35 nm)/Py or Co (20 nm)/Ru (3 nm) or Ta (5 nm) and  
112 YIG(30 nm)/Py(20 nm)/Ru(4 nm). We compare these samples to stacks grown on (110)-oriented  
113 GGG substrates with the structure Pt(10 nm)/YIG(35 nm)/Py(20 nm)/Ta(5 nm) and (111)-oriented  
114 GGG/YIG(50 nm)/Py(20 nm)/Ta(5 nm). The Pt and YIG are grown sequentially by ultra-high

115 vacuum magnetron sputtering at room-temperature, using an Ar sputtering pressure of 0.26 Pa (2  
116 mTorr). The Pt layer was grown by dc magnetron sputtering, while the YIG was grown by rf  
117 sputtering. The Si/SiO<sub>2</sub>/Pt/YIG stacks are annealed at 850 °C for 3 min in a rapid thermal annealer  
118 with sufficient oxygen flow inside. The sample was returned to vacuum to deposit a metallic FM  
119 layer, and a Ru or Ta capping layer was deposited on top of the FM layer using dc magnetron  
120 sputtering with the same temperature and pressure as the initial layers.

121 The crystal structure was primarily probed through a combination of symmetric XRD scans  
122 along the growth axis and in-plane rotation scans of Bragg reflections with both in-plane and out-  
123 of-plane components. Because the XRD provided ambiguous results from the (110)-oriented  
124 GGG/Pt/YIG/Py samples, supplemental scanning transmission electron microscopy (STEM) and  
125 electron diffraction measurements were performed on this geometry. Cross-sectional specimens  
126 were prepared by focused ion beam (FIB) lift-out. Before lift-out, protective layers of sputtered  
127 carbon followed by ion beam deposited Pt-C were applied to the surface of the thin film. Rough  
128 milling steps were performed with 30 keV Ga<sup>+</sup> ions, and the final thinning of the sample was at 5  
129 keV to reduce surface damage. High-resolution STEM experiments were then performed by a  
130 (S)TEM instrument operating with a primary beam energy of 300 keV. Annular dark field  
131 (ADF) images were acquired using a high-angle annual dark field (HAADF) detector with a  
132 convergence semi-angle of 13.7 mrad and inner collection semi-angle of approximately 60 mrad.  
133 Nanobeam electron diffraction STEM measurements were performed with a convergence semi-  
134 angle of 0.16 mrad and were collected with a 1 ms dwell time at (256 x 256) pixels per diffraction  
135 pattern with a bit depth of 12.

136 Magnetic properties are characterized by magnetometry measurements using a vibrating  
137 sample magnetometer (VSM) at room temperature, and the parallel (longitudinal,  $M_{\parallel}$ ) and

138 perpendicular (transverse,  $M_{\perp}$ ) magnetization components were measured with the applied field  
 139 in the plane of the film. First order reversal curve (FORC) measurements [19–23] were also carried  
 140 out using the same VSM in the longitudinal configuration: the sample was first saturated in a  
 141 positive magnetic field of 300 mT; then, the magnetic field ( $H$ ) was decreased to a given reversal  
 142 field ( $H_R$ ) and the magnetization,  $M(H, H_R)$ , was measured while the field was swept back to  
 143 positive saturation; this process was repeated at successively more negative  $H_R$ , creating a family  
 144 of FORCs. The normalized FORC distribution can then be calculated using the mixed second-  
 145 order derivative of the magnetization  $\rho(H_R, H) \equiv -\frac{1}{2M_s} \partial^2 M(H_R, H) / \partial H_R \partial H$ . We have  
 146 previously carried out detailed magnetometry on similar Si/SiO<sub>2</sub>/Pt/YIG/Py samples and found the  
 147 saturation magnetizations of YIG and Py were in close agreement with the bulk.

148 Depth dependence of the nuclear structure and in-plane component of the magnetization  
 149 were characterized using PNR. Data were collected using the Polarized Beam Reflectometer  
 150 (PBR) and Multi-Angle Grazing-Incidence K-vector (MAGIK) instruments at the National  
 151 Institute of Standards and Technology Center for Neutron Research (NCNR). The incident  
 152 neutrons were spin polarized parallel or antiparallel to the in-plane applied magnetic field ( $H$ ), and  
 153 reflectivity was measured with full polarization analysis ( $R^{\uparrow\uparrow}$ ,  $R^{\uparrow\downarrow}$ ,  $R^{\downarrow\uparrow}$ ,  $R^{\downarrow\downarrow}$ , where arrows indicate  
 154 the up- and down-orientation of the incident and scattered neutron spin moment) as a function of  
 155 the momentum transfer ( $Q_z$ ) normal to the surface of the film. The non-spin flip cross-sections  
 156 ( $R^{\uparrow\uparrow}$ ,  $R^{\downarrow\downarrow}$ ) are sensitive to the net magnetization component aligned with  $H$  and perpendicular with  
 157  $Q_z$ , whereas the spin flip cross-sections ( $R^{\uparrow\downarrow}$ ,  $R^{\downarrow\uparrow}$ ) probe the net magnetization perpendicular to  
 158 both  $H$  and  $Q_z$ . PNR measurements were collected at room temperature with a maximum magnetic  
 159 field of 700 mT applied along an in-plane direction of the sample. The magnetic field was first set  
 160 to 700 mT and then progressively lowered for each field state measurement. We reduced and



161 model-fit the PNR data using the REDUCTUS and REFL1D software packages,  
162 respectively [24,25]. Model-fitting of the PNR data was carried out using a slab model, in which  
163 each layer is represented as a region of uniform nuclear and magnetic scattering length density  
164 (SLD) with Gaussian interfacial roughness between adjacent layers; the model allowed for  
165 magnetic dead layers at the interfaces. For the case that a single sample was measured multiple  
166 times in different field states, the models were co-refined such that all data are fit to the same  
167 structural parameters, and only the magnetization varies with  $H$ .

168 To better understand the magnetic domain structure of the Py and Co layers with element  
169 specificity, we probed the FM layer using XPEEM with spatially resolved X-ray absorption  
170 spectroscopy (XAS) and X-ray magnetic circular dichroism (XMCD) at the Advanced Light  
171 Source PEEM3 end station (beamline 11.0.1.1). Prior to image collection, an in-plane field of 650  
172 mT was *ex situ* applied along the sample plane, and then lowered to zero. Data were collected at  
173 room temperature with X-ray illumination applied at a grazing incidence angle of  $30^\circ$ , capturing  
174 predominantly the in-plane magnetization. Measurements were performed in zero field, as is  
175 necessary for full-field PEEM. Fe, Ni, and Co,  $L_{2,3}$  absorption spectra were measured for the  
176 Si/SiO<sub>2</sub>/Pt/YIG/Ru, Si/SiO<sub>2</sub>/Pt/YIG/Py/Ru, and Si/SiO<sub>2</sub>/Pt/YIG/Co/Ta samples, respectively, to  
177 determine the energy of maximum XMCD-based contrast for imaging (Fe 709.6 eV, Ni 853 eV,  
178 Co 779 eV). The scans used to determine these energies are shown in the supplementary Figs. S9,  
179 S10, and S11. [26] Magnetic contrast images were then obtained by measuring with alternating  
180 left- and right-circularly polarized light and taking the difference in intensity between the two  
181 polarization states at the XMCD maximum energy. Images taken at a pre-edge energy were used  
182 to normalize the magnetic contrast at each polarization. Vector maps of the magnetization  
183 magnitude and direction were obtained by pixelwise fitting of data collected at four different

184 azimuthal angles ( $0^\circ$ ,  $45^\circ$ ,  $90^\circ$ , and  $180^\circ$ ). An additional Si/SiO<sub>2</sub>/Pt/YIG/Ru sample was also  
185 imaged at five different azimuthal angles ( $0^\circ$ ,  $45^\circ$ ,  $90^\circ$ ,  $135^\circ$ , and  $180^\circ$ ) to understand the domain  
186 configuration of sputtered YIG when not in contact with a ferromagnetic metal.

187

### 188 **III. RESULTS**

189

190 The  $\theta$ - $2\theta$  XRD scans on the YIG/Py and YIG/Co samples grown on Si/SiO<sub>2</sub> shown in Fig.  
191 1 reveal a highly (111)-textured Pt seed layer and polycrystalline YIG with large (420) and (422)  
192 reflections alongside a number of secondary textures such as (400), (444), (640), and (642) along  
193 the Si [001] direction. Fig. 1(a) also shows peaks consistent with (111) Py and (111) Co textures,  
194 respectively. To search for in-plane crystallographic ordering of the YIG, we rotated a sample  
195 about the film normal direction while in the Bragg condition for the (642) plane of YIG and found  
196 no evidence of strong in-plane YIG texturing. No in-plane texturing was expected since the SiO<sub>2</sub>  
197 underlayer is presumed to be amorphous and no XRD peaks for the SiO<sub>2</sub> were observed. To assess  
198 the role of the Pt seed layer, Fig. 1(a) also shows an otherwise identical sample without a Pt layer.  
199 While a shoulder persists in the YIG (420) position next to the Si (002) reflection, all YIG peaks  
200 are significantly weakened relative to the Pt-seeded samples.

201 Indeed, Table I shows the estimated volume fractions based on YIG integrated peak area  
202 and theoretical reflection intensity. There is considerable scatter in volume fraction from sample  
203 to sample, with the (420)-oriented fraction varying between 23% - 62%. The two samples grown  
204 with a Pt seed layer both exhibit (420) and (422) dominance, while the sample grown without Pt  
205 has comparable volume fractions of the (420), (422), and (642)-oriented YIG grains. We conclude,  
206 therefore, that the highly oriented Pt underlayer enhances the dominance of (420) and/or (422)  
207 texture in the YIG films in addition to improving YIG crystallinity. For relative crystallinity

208 information, see Table SI in the supporting information, which normalizes the YIG diffraction  
 209 peak intensities to the Si (004) peak intensity of each scan and reveals significant suppression of  
 210 all YIG diffraction peaks when samples are grown without a Pt layer.

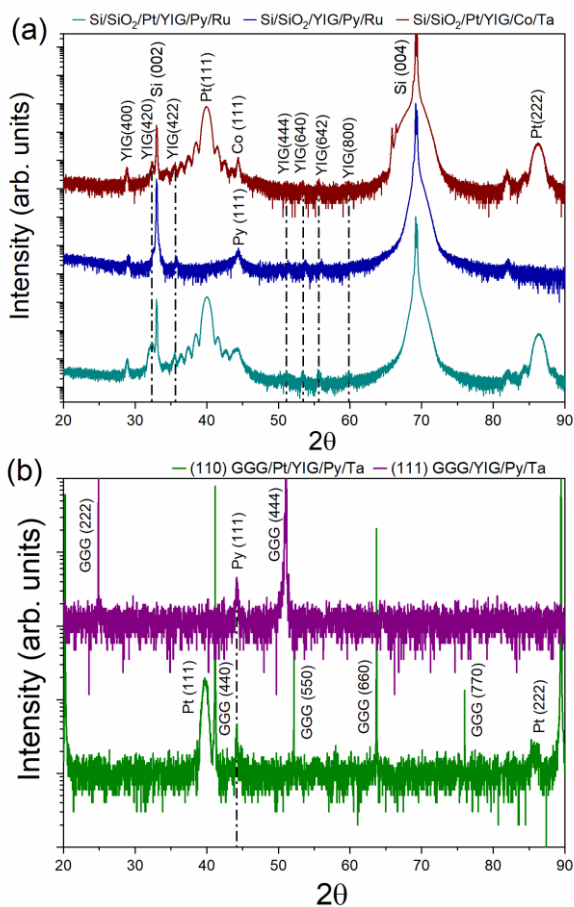
<b>Orientation</b>	<b>SiO<sub>2</sub>/Pt/YIG/Py/Ru Vol. Frac. (%)</b>	<b>SiO<sub>2</sub>/Pt/YIG/Co/Ta Vol. Frac. (%)</b>	<b>SiO<sub>2</sub>/YIG/Py/Ru Vol. Frac. (%)</b>
400	4.5	9.0	8.3
420	61.9	29.1	23.4
422	18.4	37.9	22.1
444	2.0	0	10.2
640	3.6	7.8	13.8
642	9.7	16.2	22.2

211 Table I: Summary of the estimated volume fraction of various detected crystallographic  
 212 orientations for the Si/SiO<sub>2</sub>/Pt/YIG/Py/Ru, Si/SiO<sub>2</sub>/Pt/YIG/Co/Ta, and Si/SiO<sub>2</sub>/YIG/Py/Ru  
 213 samples. Calculations based on theoretical intensities from the Inorganic Crystal Structure  
 214 Database.

215

216 Lastly, Fig. 1(b) shows XRD from (111)-oriented GGG/YIG/Py/Ta and (110)-oriented  
 217 GGG/(111)-textured Pt/YIG/Py/Ta samples. Both stack structures were designed to present a  
 218 (111)-oriented growing surface to maintain consistency with the (111)-oriented Pt grown on  
 219 amorphous SiO<sub>2</sub>. The (111)-oriented GGG/YIG represents the classic case of direct, high-quality  
 220 epitaxial YIG growth, and the expected YIG film peaks and Pendellösung fringes may be observed  
 221 for the sample on (111)-oriented GGG (see supplemental Fig. S1). On the other hand, (110)-  
 222 oriented GGG/Pt should provide an intermediate growth between the extremes of epitaxy and  
 223 amorphous SiO<sub>2</sub>. Indeed, azimuthal  $\phi$ -scans of the asymmetric GGG (642) and Pt (311) peaks,  
 224 plotted in supplemental Fig. S2, show that the GGG imparts a preferential in-plane orientation to  
 225 the Pt. However, no obvious YIG Bragg reflections or Pendellösung fringes are observable in this  
 226 sample, either from textures matching the underlying GGG or alternative crystallographic  
 227 orientations. Because previous examples of this stack geometry have shown relatively close, but

228 not perfect, alignment between the YIG and GGG, we performed STEM imaging and electron  
 229 diffraction measurements on a (110)-oriented GGG/Pt/YIG/Pt heterostructure [27]. These  
 230 measurements revealed that while the Pt interlayer does transmit preferred in-plane and out-of-  
 231 plane orientations from the GGG to the YIG, there is approximately  $2^\circ$  tilt offset between the  
 232 substrate and film (see supplemental Fig. S3). Such an offset renders the (110)-type YIG peaks  
 233 extremely difficult to locate, as the angular offset is likely to vary in both magnitude and direction  
 234 between domains, requiring extremely fine  $\phi$ - $\omega$  (azimuthal and tilt offset) mapping to observe.



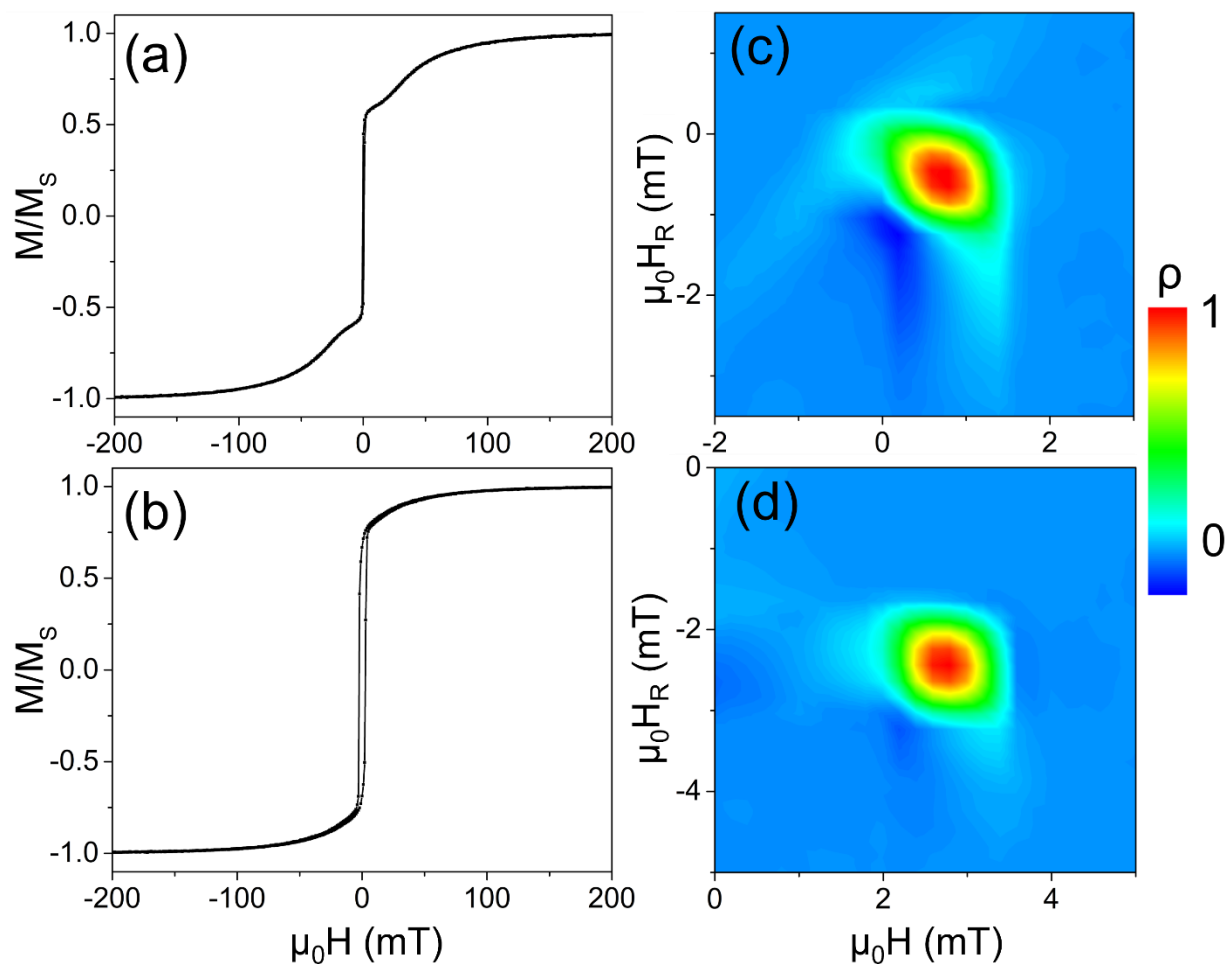
235  
 236 FIG 1: (a) Si/SiO<sub>2</sub> based heterostructures for use of Py (teal) or Co (blue) as the  
 237 ferromagnetic metal layer. Further a sample with no Pt seed layer (maroon). (b) (110)-oriented  
 238 GGG/Pt/YIG/Py/Ta and (111)-oriented GGG/YIG/Py/Ta. Dashed lines are intended to guide the  
 239 eye for subtle peaks present across multiple samples.

240

241           The room temperature longitudinal and transverse hysteresis loops [28,29] are shown in  
242 Fig. 2 and supplemental Fig. S4, respectively, for the YIG/Py and YIG/Co samples on  
243 Si/SiO<sub>2</sub>. [26,29–40] For the YIG/Py sample, as the field is decreased from positive saturation at  
244 300 mT, there is initially a gradual decrease in YIG longitudinal magnetization to achieve an anti-  
245 parallel alignment between the YIG and the Py (Fig. 2a), as shown by previously reported PNR  
246 results. [18] Subsequently, application of a small negative field yields a sharp switching associated  
247 with the Py layer reversal, along with a coercivity of 0.7 mT; presumably the YIG also reverses,  
248 now pointing in a positive orientation, to maintain its antiparallel alignment. [41] Based on the  
249 magnetization and given the thicknesses and saturation moment determined previously [18] the  
250 YIG is not fully reversed at the coercive field and may contain domains, reducing the net  
251 magnetization. At more negative fields, the YIG is gradually forced into alignment with the applied  
252 field, although a very small slope persists through the entire measurement range. For the YIG/Co  
253 sample, the longitudinal moment exhibits a similar trend with magnetic field as the YIG/Py  
254 sample, except for differences in the loop shape and a relatively larger low-field switching  
255 component with an  $M/M_s$  of  $\approx 0.78$  before switching [Fig. 2(b)].

256           FORC distributions for the YIG/Py and YIG/Co samples are shown in Fig. 2(c) and 2(d),  
257 displaying a single peak at  $(H, H_R)$  of (0.7, -0.5) mT and (2.7, -2.4) mT, respectively. The  
258 associated families of FORCs and full field range FORC distributions are shown in supplementary  
259 Fig. S5 [26]. Interestingly, we find that the FORC distributions for both YIG/Py and YIG/Co  
260 samples to be featureless except near the soft layer switching fields. Reviewing the full-range  
261 FORC diagram, shown in the Supplemental Material Fig. S5, the low-field features in Fig. 2(c)  
262 and 2(d) are the only non-zero contributions to the FORC diagram, indicating that the switching

263 of the YIG layer at higher fields is mostly reversible. [26] The FORC features in Fig. 2(c) and 2(d)  
 264 are associated with the irreversible Py or Co layer switching and indicate reversal by domain  
 265 nucleation and propagation [38,42].



266  
 267 Fig. 2: (a,b) In-plane longitudinal hysteresis loops and (c,d) FORC distribution for a (a,c)  
 268 Si/SiO<sub>2</sub>/Pt/YIG/Py/Ru and (b,d) Si/SiO<sub>2</sub>/Pt/YIG/Co/Ta sample, respectively.

269  
 270 To directly probe the magnetization in the Si/SiO<sub>2</sub>/Pt/YIG/FM heterostructures, we make  
 271 use of PNR to measure the depth profile of the chemical composition and the net in-plane  
 272 magnetization. A summary of our previously reported PNR data and model-fitting of the

273 Si/SiO<sub>2</sub>/Pt/YIG/Py/Ru is presented in ref. 18. In that work, scattering length density profiles  
274 corresponding to the best fits indicated parallel alignment of YIG and Py at magnetic fields above  
275 150 mT. Below 150 mT, the YIG begins to reorient into an antiparallel configuration with respect  
276 to  $H$  and Py. Our previous PNR investigation of comparable-thickness Si/SiO<sub>2</sub>/Pt/YIG/Py/Ru  
277 samples also revealed chemical compositions near theoretical bulk values, sharp interfaces,  
278 magnetic depth profiles in strong agreement with the magnetometry, and a lack of any statistically  
279 significant magnetic dead layer [18]. While spin-flip data were collected in this study, no  
280 statistically significant signals were observed after polarization correction, indicating the absence  
281 of a significant net in-plane magnetization perpendicular to the applied field.

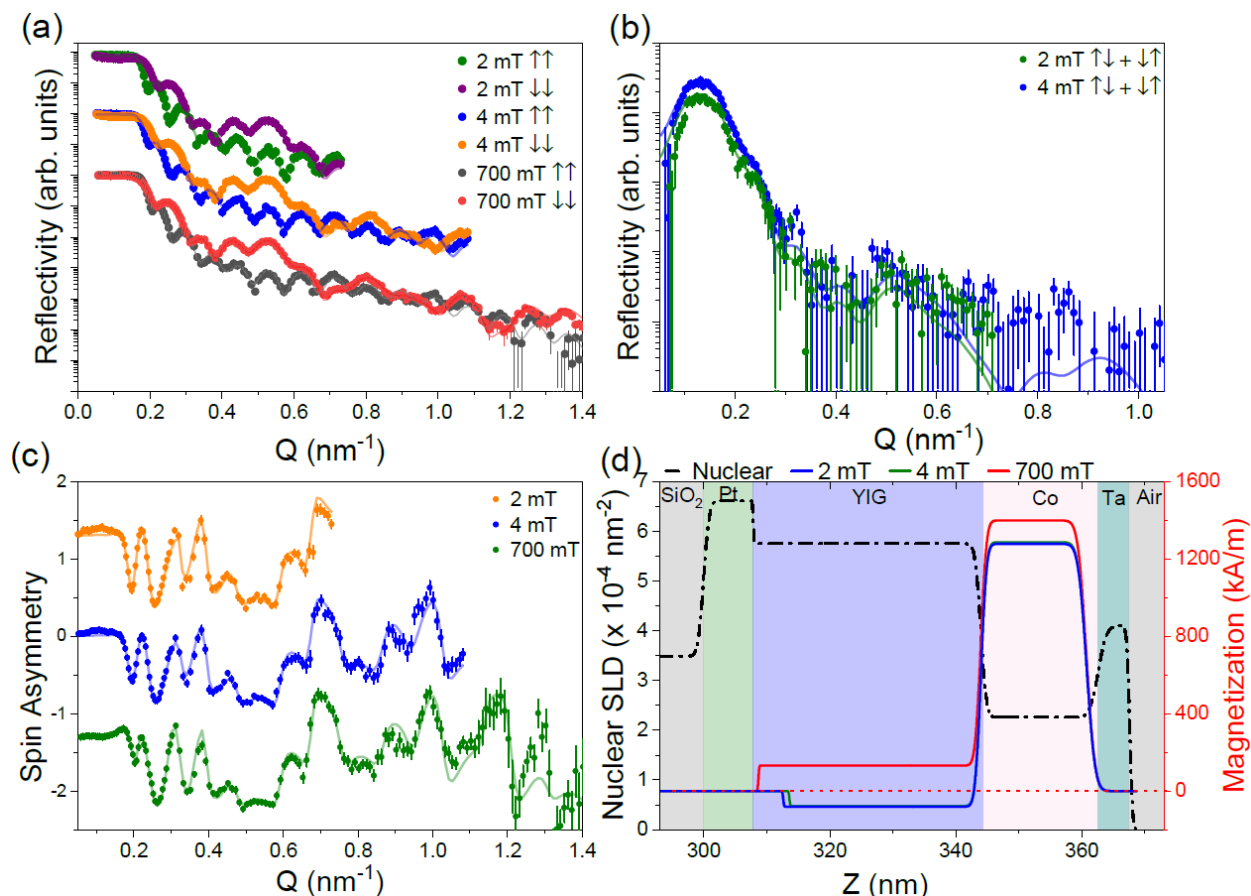
282 To determine the generality of antiparallel coupling at YIG/FM interfaces for samples  
283 grown on Si/SiO<sub>2</sub>, we probed a Si/SiO<sub>2</sub>/Pt/YIG/Co/Ta heterostructure with PNR. The fitted non-  
284 spin-flip PNR cross sections from this sample at  $H = 700$  mT, 4 mT, and 2 mT are shown in Fig.  
285 3a. Non-zero spin-flip scattering was observed at both 4 mT and 2 mT, and these cross-sections  
286 are shown alongside theoretical fits in Fig. 3b. To illustrate the relative scaling of the spin-flip and  
287 non-spin-flip signals, they are plotted on the same scale for the 4 mT condition in Fig. S7. The  
288 non-zero spin-flip measurements imply a net in-plane moment orthogonal to the guide field in the  
289 4 mT and 2 mT measurements which, as discussed above, may be the result of subtle growth  
290 morphology effects which may occur even in films without in-plane texturing. [43,44] Low-field  
291 data were therefore fit using models which allowed the direction of the net in-plane moment in  
292 both the YIG and Co layers to independently rotate away from the applied field. The fitted spin  
293 asymmetry ( $SA = \frac{R^{++}-R^{--}}{R^{++}+R^{--}}$ ), which emphasizes the scattering contributions of the net  
294 magnetization parallel to the magnetic field, is plotted in Fig. 3c. The scattering length density  
295 profiles corresponding to the best fits to the data are shown in Fig. 3d and reveal sharp interfaces,

296 nuclear and magnetic scattering length densities in close agreement with expected values, and no  
297 magnetic dead layers at 700 mT apart from a small region at the top surface of the Co layer.  
298 Describing the low-field data required mostly antiparallel alignment of the YIG and Co moments,  
299 with angles of  $161(2)^\circ$  and  $153(2)^\circ$  between the YIG and Co moments at 2 mT and 4 mT,  
300 respectively;  $180^\circ$  denotes fully antiparallel in-plane alignment. The fitted YIG magnetization at  
301 2 mT and 4 mT is 61(4) % and 58(3) % of the 700 mT saturated value, respectively, suggesting  
302 that the YIG likely forms partially cancelling domains with a weak perpendicular component to  
303 the magnetization. This agrees with the previously reported behavior at the YIG/Py interface, in  
304 which approximately 76 % of the moment is recovered in the antiparallel YIG at 4 mT. In contrast  
305 to the Py magnetization in Si/SiO<sub>2</sub>/Pt/YIG/Py/Ru samples, the Co magnetization in  
306 Si/SiO<sub>2</sub>/Pt/YIG/Co/Ta is found to rotate away from the applied field by as much as  $10.55(5)^\circ$  at  
307 low-field; this rotation is proposed to be the result of an as-of-yet unidentified in-plane anisotropy.  
308 The magnetization data (Fig. S4) provide further evidence of this weak uniaxial anisotropy.  
309 Though the Co-film has no net in-plane crystalline orientation, we speculate that microstructural  
310 effects may be responsible for this effect. [39,40,43]

311 We note that one feature in the PNR of Si/SiO<sub>2</sub>/Pt/YIG/Co/Ta is extremely difficult to  
312 account for in the fitting. A splitting appears between the two non-spin flip cross sections below  
313 the critical edge at low field. While a feature of this type is expected due to the large magnetic  
314 moment and slightly larger (relative to Fe or Ni) neutron absorption cross section of Co, the effect  
315 is too large to originate solely from these factors. Instead, we posit that domain formation driven  
316 by Co-anisotropy leads to off-specular scattering which acts to preferentially remove intensity  
317 primarily from one of the non-spin-flip cross sections [33,45]. We confirm this hypothesis by  
318 performing a series of rocking curves on the sample at different  $Q_z$  values to identify the associated



319 off-specular reflections. Some modifications in the standard data treatment are required to address  
 320 these effects in the PNR analysis to account for this and are discussed in detail in the supplemental  
 321 information. [26]



322  
 323 Fig. 3: (a) Non spin-flip PNR data and theoretical fits for the Si/SiO<sub>2</sub>/Pt/YIG/Co/Ta sample at 700  
 324 mT, 4 mT, and 2 mT. (b) Spin-flip reflectivities at 4 mT and 2 mT with theoretical fits. (c) Spin  
 325 asymmetries and fits at 700 mT, 4 mT, and 2 mT. (d) Nuclear and magnetic depth profiles used to  
 326 generate the fits shown. Note that the low-field canting angles of the magnetization discussed in  
 327 the text are not shown. Error bars indicate single standard deviation uncertainties based on  
 328 counting statistics.

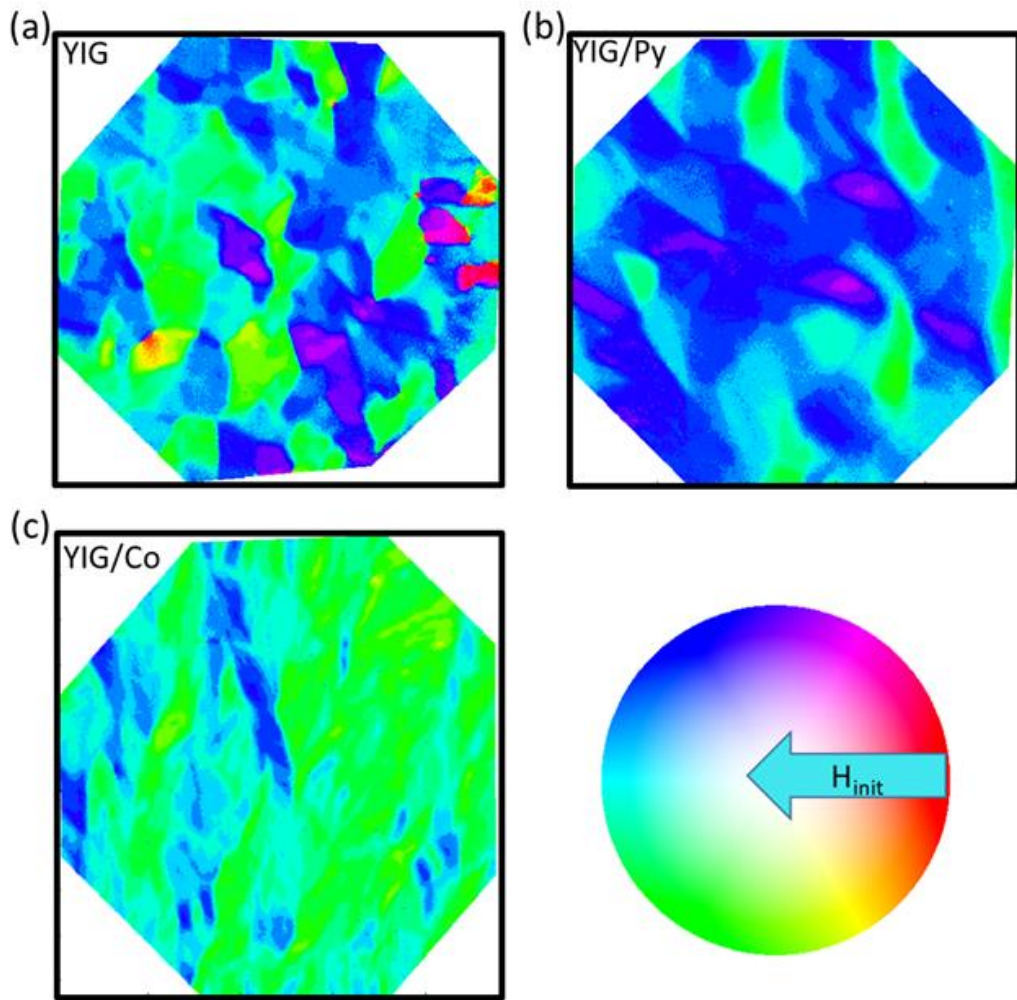
329  
 330 We obtained a more detailed understanding of different domain structures in YIG/Py and  
 331 YIG/Co grown on Si/SiO<sub>2</sub>/Pt using magnetic domain imaging with X-PEEM. Fig. 4 shows in-  
 332 plane vector magnetometry maps obtained by using five XMCD PEEM images taken at 0°, 45°,  
 333 90°, 135°, and 180° to pixelwise fit the magnetization directions in each field of view in a bare

334 YIG/Ru film, a YIG/Py/Ru film, and a YIG/Co/Ta film, all grown on Si/SiO<sub>2</sub>/Pt. While 3 angles  
335 (e.g. 0°, 90°, and 180°) are sufficient to determine the three dimensional magnetization orientation  
336 in the field of view, additional images at intermediate angles were used in the fitting for better  
337 statistical confidence in the pixelwise fits. Here we note that the images shown for YIG, YIG/Py,  
338 and YIG/Co were taken using the Fe, Ni, and Co L<sub>3</sub> edges as described in the methods and  
339 supplemental information. [26] The L<sub>2,3</sub> absorption spectra for Co on the YIG/Co sample, and Fe  
340 and Ni on the YIG and YIG/Py samples, respectively, are shown in supplementary Figs. S9, S10,  
341 and S11, respectively [26], and indicate no significant oxidation of the surface Co or Py [46]. The  
342 thicknesses of the Py and Co layers were well beyond the photoelectron escape depth of  
343 approximately 5 nm, so that it was not possible to image the underlying YIG, and we instead use  
344 a bare YIG film for comparison. Further, it is critical to recall the extremely weak anisotropy of  
345 Py. Since the PNR measurements required a magnetic field of at least 1 mT to maintain neutron  
346 polarization while the X-PEEM must be done in zero-field, the domain state of the Py (and  
347 consequently the underlying YIG) may be very different for the PNR and XPEEM measurements.  
348 That being said, the PEEM data confirms the PNR observation that the Py and Co layers dominate  
349 the magnetization, aligning mostly parallel to the initializing field at remanence.

350         Nevertheless, key insights may be gleaned by comparing the images in Fig. 4. Specifically,  
351 the YIG and Py domains appear to have very similar morphology, indicating that the YIG domain  
352 structure is being imprinted onto the permalloy, with domains  $\approx 2 \mu\text{m}$  to  $5 \mu\text{m}$  in their lateral  
353 dimensions. These images also show that the YIG and YIG/Py samples have no significant  
354 asymmetry in the reversal directions. In contrast to the lack of a preferred direction in the Py, the  
355 Co image shows a significantly different magnetic domain structure, with widths parallel to the  
356 conditioning field of  $\approx 5 \mu\text{m}$ , but lengths orthogonal to the field of  $>20 \mu\text{m}$ . This domain structure

357 is consistent with a uniaxial anisotropy induced in Co through microstructural effects induced by  
358 the growth morphology, emphasizing that while the coupling across the interface is similar across  
359 different FM systems, the low-field behavior may be tuned by varying materials choice and growth  
360 parameters. [39,40,43]

361

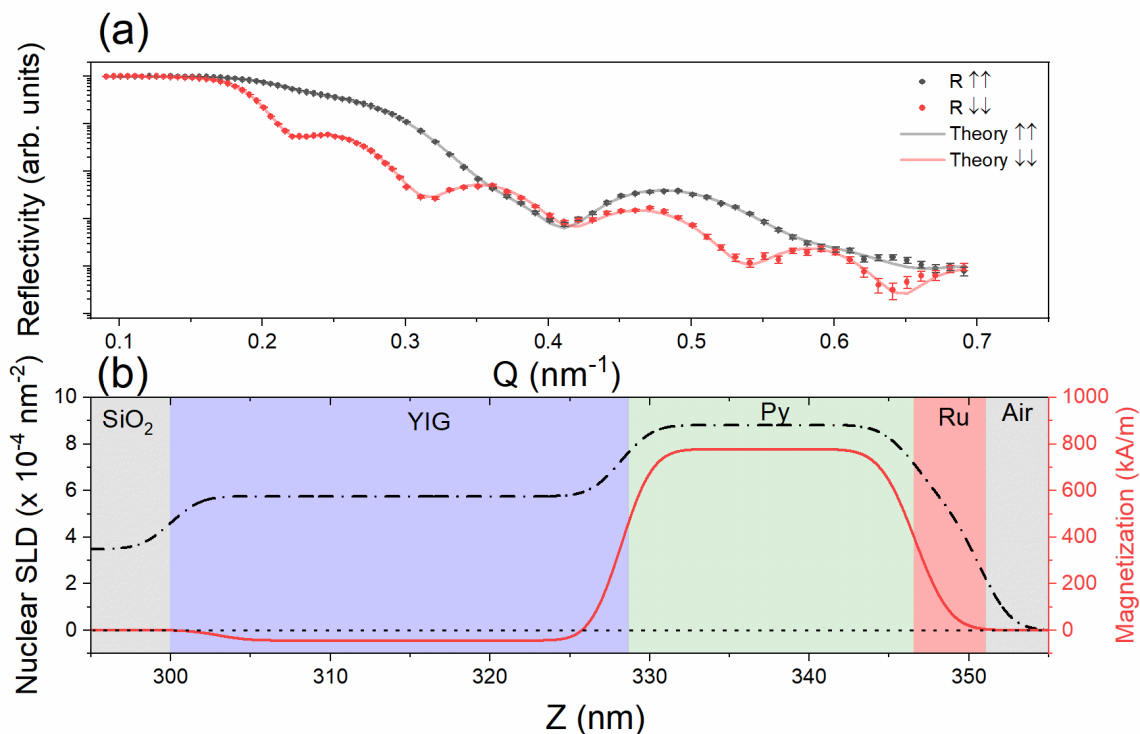


362

363 Fig. 4: In-plane magnetic moment orientation determined from XMCD-PEEM data at the  $L_3$  edge  
364 of (a) Fe on the Si/SiO<sub>2</sub>/Pt/YIG/Ru (b) Ni on the Si/SiO<sub>2</sub>/Pt/YIG/Py/Ru sample and (c) Co on the  
365 Si/SiO<sub>2</sub>/Pt/YIG/Co/Ta sample. The field of view for all images is 28  $\mu\text{m}$ . (d) Color mapping of  
366 the in-plane moment angle in (a), (b), and (c).

367

368 Having demonstrated that the antiparallel alignment of the YIG and FM layers at low field  
 369 appears to be a generalizable behavior in Si/SiO<sub>2</sub>/Pt/YIG/FM structures, we may better understand  
 370 the fundamental underpinnings by turning our attention to alternative structures. We performed  
 371 PNR at 700 mT and 4 mT on a Si/SiO<sub>2</sub>/YIG/Py/Ru structure in which the YIG is grown without a  
 372 Pt seed layer. The 4 mT measurement and the associated best-fit depth profile are shown in Fig. 5.  
 373 Once again, we find high-quality interfaces, bulk-like scattering length densities, and antiparallel  
 374 alignment of the YIG and Py. The lack of a Pt seed layer appears to suppress the magnetization in  
 375 the YIG layer, likely as a result of the reduced crystallinity revealed by the x-ray diffraction of Fig.  
 376 1. Nevertheless, approximately 80 % of the saturated YIG magnetization appears to be aligned  
 377 antiparallel at 4 mT in this sample, suggesting that it is not the YIG crystal quality which  
 378 determines the sign of the interface exchange coupling.

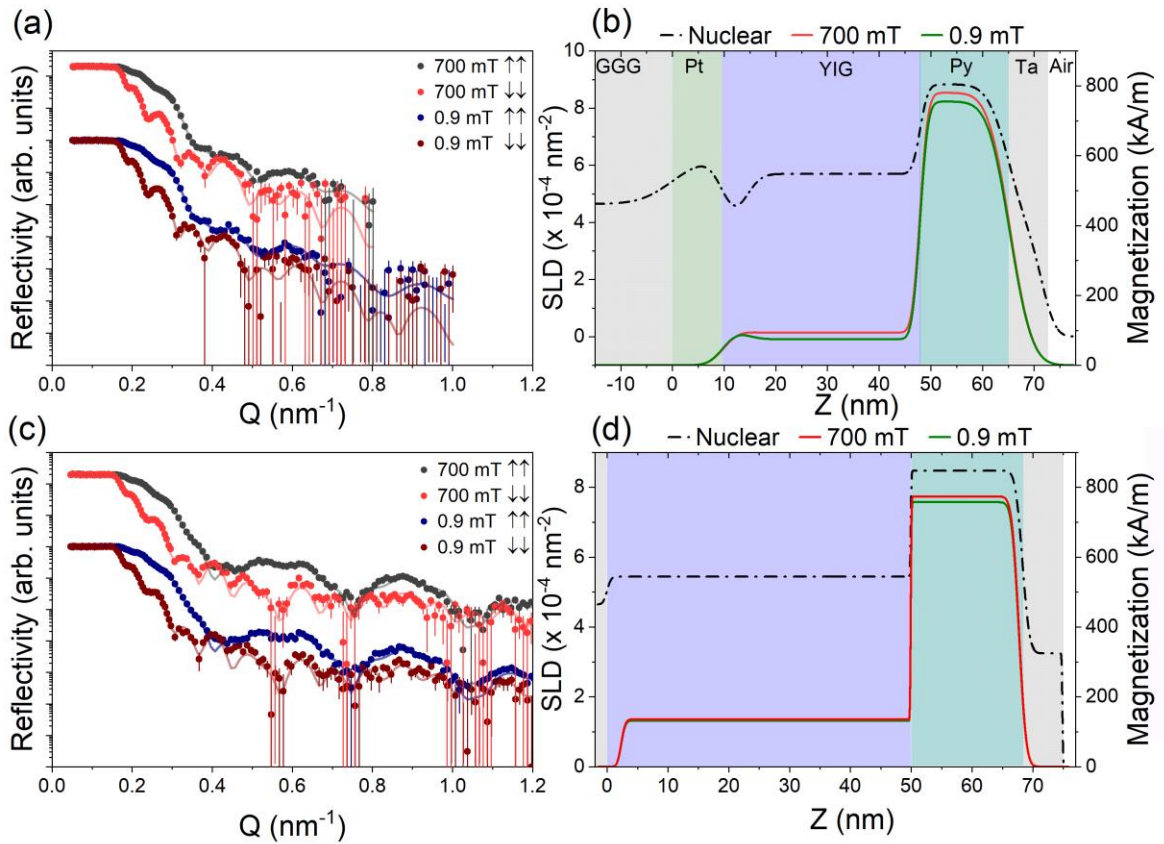


379

380 Fig. 5: (a) Non spin-flip PNR data and theoretical fits for a Si/SiO<sub>2</sub>/YIG/Py/Ru sample at 4 mT.  
381 (b) Non-spin-flip reflectivities at 4 mT and with theoretical fits. (b) Nuclear (black, dash-dot, left  
382 axis) and magnetic (red, solid, right axis) depth profiles used to generate the fits shown. Error bars  
383 indicate single standard deviation uncertainties based on counting statistics.

384  
385 Since crystal quality appeared not to be the decisive factor in the observed  
386 antiferromagnetic coupling, we also probed the role of crystallographic orientation by measuring  
387 PNR on a pair of YIG/Py samples grown on GGG with and without a Pt seed layer. In Fig. 6, we  
388 show the measured PNR, model-fits, and spin asymmetry for both of these samples, which had  
389 nominal structures of (110) GGG /Pt (10 nm)/YIG (35 nm)/Py (20 nm)/Ta (5 nm) and (111)  
390 GGG/YIG (50 nm)/Py (20 nm)/Ta (5 nm), measured at 700 mT and 0.9 mT. In both cases, we find  
391 only minor changes in the magnetic depth profile between high and low field measurements, and  
392 a clear absence of the antiparallel coupling that is seen in the Si/SiO<sub>2</sub> based samples. This  
393 conclusion is reinforced by the near perfect overlap of the spin asymmetry at both field conditions  
394 (see Fig. S8 in the supplemental information). [26] While this result is well reported in the  
395 literature, it remains quite interesting in that it highlights that exchange coupling between YIG and  
396 well-known ferromagnetic metals is tied to the sample design in a non-trivial way.

397 Of further interest is the resulting magnetic depth profiles near the (111) GGG/YIG and  
398 (110) GGG/Pt/YIG interfaces in the two samples. While the (111) GGG/YIG sample exhibits a  
399 room-temperature magnetic dead layer in the first few nanometers of the YIG layer, this feature is  
400 absent in the GGG/Pt/YIG, despite a lower-density transitional growth region in the latter sample.  
401 The dead layer observed at the direct GGG/YIG interface is consistent with varying reports of a  
402 structural and magnetic reconfiguration associated with interdiffusion in the relatively open garnet  
403 structures [16,17,47]. We speculate that the Pt may act as an effective diffusion barrier while  
404 simultaneously preserving a highly oriented crystal structure on which to grow high-quality YIG.



406

407 Fig. 6: (a) PNR data and model-fits for (110) GGG/Pt(10 nm)/YIG(35 nm)/Py(20 nm)/Ta(5 nm)  
 408 collected at 700 mT and 0.9 mT. (b) Nuclear scattering length density profiles (left axis, dash-dot)  
 409 and magnetization depth profile (right axis, solid) obtained from model-fitting the PNR data in (a).  
 410 (c) PNR data and model-fits for (111) GGG/YIG(50 nm)/Py(20 nm)/Ta(5 nm) with associated  
 411 depth profiles in (d). Note that  $Z = 0$  nm refers to the surface of the GGG substrate. Error bars  
 412 indicate single standard deviation uncertainties based on counting statistics.

413

#### 414 IV. DISCUSSION

415

416

In the introduction, we posited that a complex interplay of many factors was likely to play  
 417 a role in determining the sign of interface coupling at the YIG/FM interface. Specifically, we  
 418 identified surface termination, FM choice, structural disorder, and deposition technique selection  
 419 as potential factors. In this work, we narrowed the range of possible explanations through the

420 application of XRD, magnetometry, PNR, XPEEM, and STEM to a range of sample designs,  
 421 summarized in Table II, that provides a more comprehensive understanding of interfacial magnetic  
 422 coupling in YIG/FM heterostructures.

Sample	YIG Orientation	Coupling	Anisotropy
Si/SiO <sub>2</sub> /Pt/YIG/Co/Ta	Textured	Antiferromagnetic	Strong
Si/SiO <sub>2</sub> /Pt/YIG/Py/Ru [18]	Textured	Antiferromagnetic	Weak
Si/SiO <sub>2</sub> /YIG/Py/Ru	Polycrystalline	Antiferromagnetic	Weak
(111) GGG/YIG/Py/Ta	(111)	Ferromagnetic	Weak
(110) GGG/Pt/YIG/Py/Ta	(110)	Ferromagnetic	Weak

423 Table II: Summary of sample geometries and the resulting orientations, magnetic  
 424 couplings, and anisotropy observed.

425

426 We show that the antiparallel interface coupling is preserved when substituting Co for Py,  
 427 leading us to suspect that the antiparallel coupling results from direct transition metal to  
 428 ferromagnetic metal exchange at the interface rather than a very specific superexchange interaction  
 429 unique to YIG/Py. Further, we found that the antiparallel exchange coupling is preserved in  
 430 samples with sharply reduced YIG crystallinity for samples grown on SiO<sub>2</sub> without a Pt seed layer.  
 431 In contrast, any growth stack resulting in a highly in-plane oriented or epitaxial YIG film coupled  
 432 ferromagnetically across the interface. This is true for YIG grown on both (111) GGG, where the  
 433 YIG matches the underlying orientation of the substrate, and (110) GGG/Pt, where the YIG is  
 434 relatively (110)-oriented albeit with some tilt misalignment and lower crystal quality. This  
 435 combination of observations tends to rule out FM choice, disorder, and deposition-specific issues  
 436 while implicating the surface termination of the YIG films.

437           However, the observations of S. Klingler *et al.* remain challenging to reconcile.  
438 Specifically, while our high-quality (111) GGG/(111) YIG/FM layers support ferromagnetic YIG-  
439 FM exchange, the (111)-GGG/YIG/Co in Klingler *et al.* shows indications of some form of  
440 antiparallel alignment. [8] We speculate that the surface terminations of these two samples may be  
441 very different, as Klingler *et al.* follow a YIG surface preparation approach from S. Pütter *et al.*  
442 which is known to alter the relative surface concentrations of Y, Fe, and O in favor of relatively  
443 higher Y and O concentrations. [48] These observations are, therefore, consistent with a picture of  
444 YIG/FM interface coupling which is highly sensitive to the interface configuration.

445           Having identified the likely source of anomalous magnetic coupling in the system, we may  
446 identify several likely candidate textures. YIG layers grown on amorphous SiO<sub>2</sub> exhibit primarily  
447 (420), (422), and (642) orientations with or without a Pt seed layer. [27] Some weaker textures  
448 observable in these samples include the (400), (444), and (640), but for samples with a Pt seed the  
449 volume fraction of these is sufficiently low that they are unlikely to contribute significantly the  
450 exchange. We regard the (420) and (422) orientations as the most likely origins of the antiparallel  
451 coupling, given that these textures have consistently high volume fractions across all samples. The  
452 coexistence of many grain boundaries and different orientations on the YIG surface may also give  
453 rise to frustration and surface reconstruction, and the role of these effects is challenging to separate.  
454 Indeed, the details of the surface morphology and termination can lead to antiparallel exchange  
455 coupling even in highly oriented garnet films, as recently reported for Tm<sub>3</sub>Fe<sub>5</sub>O<sub>12</sub>/W  
456 interfaces. [49] Given the surface sensitivity of the interfacial exchange coupling, either surface  
457 termination effects or microstructure induced frustration remain plausible explanations and further  
458 work is required.



459           Lastly, we note differences in the reversal behavior of Co and Py, which indicate that  
460 anisotropy plays a role in the low-field configuration at the YIG/Co interface. As explored above,  
461 this anisotropy is unexpected in samples grown without significant in-plane texture, but Co  
462 anisotropy has been demonstrated in similar systems and is typically attributed to the specifics of  
463 the growth-dependent microstructure. [39,40,43] While we expect such behavior to vary  
464 considerably depending on the specific growth conditions used, it does represent an additional  
465 tuning parameter for use in the design of hybrid YIG/FM heterostructures for magnon spintronics.  
466 Specifically, the differences in anisotropy appear to lead to pronounced contrasts in the in-plane  
467 domain structure at low-fields as determined by PEEM and verified by low-Q PNR features. While  
468 the YIG domain structure appears to imprint on an adjacent Py layer, this is not true of the Co,  
469 where a fine-structured uniaxial domain pattern emerges instead.

470

## 471 **V. CONCLUSIONS**

472           In summary, we have carried out detailed characterization and analysis of the coupling and  
473 switching methods in Si and GGG-based YIG/FM hybrid structures. The antiparallel coupling  
474 between YIG and ferromagnetic metals is confirmed for both Py and Co on films grown Si/SiO<sub>2</sub>/Pt.  
475 We further show that this preferential antiferromagnetic coupling is independent of the presence  
476 of a Pt seed layer for YIG growth and that the antiparallel coupling may be related to either certain  
477 dominant YIG film textures or the presence of disorder/grain boundaries at the YIG surface.  
478 Finally, we find that the antiparallel coupling does not manifest in analogous but highly oriented  
479 samples grown on (111) GGG and (110) GGG/Pt substrates with or without a Pt seed layer. These  
480 results implicate the termination surface in the YIG as the origin of the antiparallel mechanism.  
481 Lastly, we note that subtle differences were observed in the evolution of the low-field domain

482 structure, including an in-plane anisotropy which dominates the Co orientation at low fields, which  
483 provides another potential knob through which to control the efficiency of magnon spin valve  
484 efficiencies in garnet/metallic ferromagnet heterostructures.

485

## 486 **ACKNOWLEDGEMENTS**

487         Research was performed in part at the NIST Center for Nanoscale Science and Technology.  
488 This research was partially supported by National Science Foundation, through the Massachusetts  
489 Institute of Technology Materials Research Science and Engineering Center (DMR-1419807) and  
490 at Georgetown University (ECCS-1933527, ECCS-2151809), and by SMART, one of seven  
491 centers of nCORE, a Semiconductor Research Corporation program, sponsored by National  
492 Institute of Standards and Technology (NIST). DAG is partly supported by the DOE office of  
493 Basic Research, Award DE-SC0021344 This research used resources of the Advanced Light  
494 Source, which is a DOE Office of Science User Facility under contract no. DE-AC02-05CH11231.

495

496 **REFERENCES**

- 497 [1] Y. Kajiwara K. Harii, S. Takahashi, J. Ohe, K. Uchida, M. Mizuguchi, H. Umezawa, H. Kawai,  
 498 K. Ando, K. Takanashi, S. Maekawa, and E. Saitoh, *Transmission of Electrical Signals by*  
 499 *Spin-Wave Interconversion in a Magnetic Insulator*, Nature **464**, 262 (2010).
- 500 [2] M. Wu and A. J. Hoffman, *Recent Advances in Magnetic Insulators: From Spintronics to*  
 501 *Microwave Applications* (Academic Press, 2013).
- 502 [3] L. J. Cornelissen, J. Liu, R. A. Duine, J. ben Youssef, and B. J. van Wees, *Long-Distance*  
 503 *Transport of Magnon Spin Information in a Magnetic Insulator at Room Temperature*, Nat  
 504 Phys **11**, 1022 (2015).
- 505 [4] B. L. Giles, Z. Yang, J. S. Jamison, and R. C. Myers, *Long-Range Pure Magnon Spin Diffusion*  
 506 *Observed in a Nonlocal Spin-Seebeck Geometry*, Phys Rev B **92**, 224415 (2015).
- 507 [5] W. Jiang, P. Upadhyaya, Y. Fan, J. Zhao, M. Wang, L.-T. Chang, M. Lang, K. L. Wong, M.  
 508 Lewis, Y.-T. Lin, J. Tang, S. Cherepov, X. Zhou, Y. Tserkovnyak, R. N. Schwartz, and K. L.  
 509 Wang, *Direct Imaging of Thermally Driven Domain Wall Motion in Magnetic Insulators*,  
 510 Phys Rev Lett **110**, 177202 (2013).
- 511 [6] A. v. Chumak, V. I. Vasyuchka, A. A. Serga, and B. Hillebrands, *Magnon Spintronics*, Nat  
 512 Phys **11**, 453 (2015).
- 513 [7] H. Yu, J. Xiao, and P. Pirro, “*Magnon Spintronics*,” J Magn Magn Mater **450**, 1 (2018).
- 514 [8] S. Klingler V. Amin, S. Geprägs, K. Ganzhorn, H. Maier-Flaig, M. Althammer, H. Huebl, R.  
 515 Gross, R. D. McMichael, M. D. Stiles, S. T. B. Goennenwein, and M. Weiler, *Spin-Torque*  
 516 *Excitation of Perpendicular Standing Spin Waves in Coupled YIG/Co Heterostructures*, Phys  
 517 Rev Lett **120**, 127201 (2018).
- 518 [9] J. Chen, C. Liu, T. Liu, Y. Xiao, K. Xia, G. E. W. Bauer, M. Wu, and H. Yu, *Strong Interlayer*  
 519 *Magnon-Magnon Coupling in Magnetic Metal-Insulator Hybrid Nanostructures*, Phys Rev  
 520 Lett **120**, 217202 (2018).
- 521 [10] H. Qin, S. J. Hämäläinen, and S. van Dijken, *Exchange-Torque-Induced Excitation of*  
 522 *Perpendicular Standing Spin Waves in Nanometer-Thick YIG Films*, Sci Rep **8**, 5755 (2018).
- 523 [11] E. Lee-Wong, R. Xue, F. Ye, A. Kreisel, T. van der Sar, A. Yacoby, and C. R. Du, *Nanoscale*  
 524 *Detection of Magnon Excitations with Variable Wavevectors Through a Quantum Spin*  
 525 *Sensor*, Nano Lett **20**, 3284 (2020).
- 526 [12] Z. Zhang, M. O. Scully, and G. S. Agarwal, *Quantum Entanglement between Two Magnon*  
 527 *Modes via Kerr Nonlinearity Driven Far from Equilibrium*, Phys Rev Res **1**, 023021 (2019).
- 528 [13] R. G. E. Morris, A. F. van Loo, S. Kosen, and A. D. Karenowska, *Strong Coupling of Magnons*  
 529 *in a YIG Sphere to Photons in a Planar Superconducting Resonator in the Quantum Limit*,  
 530 Sci Rep **7**, 11511 (2017).

- 531 [14] H. Wu, L. Huang, C. Fang, B. S. Yang, C. H. Wan, G. Q. Yu, J. F. Feng, H. X. Wei, and X. F.  
532 Han, *Magnon Valve Effect between Two Magnetic Insulators*, Phys Rev Lett **120**, 097205  
533 (2018).
- 534 [15] J. Cramer, F. Fuhrmann, U. Ritzmann, V. Gall, T. Niizeki, R. Ramos, Z. Qiu, D. Hou, T.  
535 Kikkawa, J. Sinova, U. Nowak, E. Saitoh, and M. Kläui, *Magnon Detection Using a Ferroic*  
536 *Collinear Multilayer Spin Valve*, Nat Commun **9**, 1089 (2018).
- 537 [16] A. Mitra, O. Cespedes, Q. Ramasse, M. Ali, S. Marmion, M. Ward, R. M. D. Brydson, C. J.  
538 Kinane, J. F. K. Cooper, S. Langridge, and B. J. Hickey, *Interfacial Origin of the*  
539 *Magnetisation Suppression of Thin Film Yttrium Iron Garnet*, Sci Rep **7**, 11774 (2017).
- 540 [17] S. M. Sutorin, A. M. Korovin, B. E. Bursian, L. V. Lutsev, V. Bourobina, N. L. Yakovlev, M.  
541 Montecchi, L. Pasquali, V. Ukleev, A. Vorobiev, A. Devishvili, and N. S. Sokolov, *Role of*  
542 *Gallium Diffusion in the Formation of a Magnetically Dead Layer at the*  
543 *Y3Fe5O12/Gd3Ga5O12 Epitaxial Interface*, Phys Rev Mater **2**, 104404 (2018).
- 544 [18] Y. Fan, P. Quarterman, J. Finley, J. Han, P. Zhang, J. T. Hou, M. D. Stiles, A. J. Grutter, and L.  
545 Liu, *Manipulation of Coupling and Magnon Transport in Magnetic Metal-Insulator Hybrid*  
546 *Structures*, Phys Rev Appl **13**, 061002 (2020).
- 547 [19] E. C. Burks, D. A. Gilbert, P. D. Murray, C. Flores, T. E. Felter, S. Charnvanichborikarn, S. O.  
548 Kucheyev, J. D. Colvin, G. Yin, and K. Liu, *3D Nanomagnetism in Low Density*  
549 *Interconnected Nanowire Networks*, Nano Lett **21**, 716 (2021).
- 550 [20] M. T. Rahman, R. K. Dumas, N. Eibagi, N. N. Shams, Y.-C. Wu, K. Liu, and C.-H. Lai,  
551 *Controlling Magnetization Reversal in Co/Pt Nanostructures with Perpendicular*  
552 *Anisotropy*, Appl Phys Lett **94**, 042507 (2009).
- 553 [21] J. E. Davies, O. Hellwig, E. E. Fullerton, G. Denbeaux, J. B. Kortright, and K. Liu,  
554 *Magnetization Reversal of CoPt Multilayers: Microscopic Origin of High-Field Magnetic*  
555 *Irreversibility*, Phys Rev B **70**, 224434 (2004).
- 556 [22] C. R. Pike, A. P. Roberts, and K. L. Verosub, *Characterizing Interactions in Fine Magnetic*  
557 *Particle Systems Using First Order Reversal Curves*, J Appl Phys **85**, 6660 (1999).
- 558 [23] D. A. Gilbert, G. T. Zimanyi, R. K. Dumas, M. Winklhofer, A. Gomez, N. Eibagi, J. L. Vicent,  
559 and K. Liu, *Quantitative Decoding of Interactions in Tunable Nanomagnet Arrays Using*  
560 *First Order Reversal Curves*, Sci Rep **4**, 4204 (2014).
- 561 [24] B. J. Kirby, P. A. Kienzle, B. B. Maranville, N. F. Berk, J. Krycka, F. Heinrich, and C. F.  
562 Majkrzak, *Phase-Sensitive Specular Neutron Reflectometry for Imaging the Nanometer*  
563 *Scale Composition Depth Profile of Thin-Film Materials*, Curr Opin Colloid Interface Sci **17**,  
564 44 (2012).
- 565 [25] B. Maranville, W. Ratcliff II, and P. Kienzle, *Reductus : A Stateless Python Data Reduction*  
566 *Service with a Browser Front End*, J Appl Crystallogr **51**, 1500 (2018).
- 567 [26] *The Supplemental Information Contains Additional Details on X-Ray Diffraction, Electron*  
568 *Microscopy, Vector Magnetometry and First Order Reversal Curve Measurements, as Well*

- 569 *as an Expanded Analysis of the Polarized Neutron Reflectometry Data and Background X-*  
570 *Ray Photoemission Electron Microscopy Data.*
- 571 [27] Y. Fan, J. Finley, J. Han, M. E. Holtz, P. Quarterman, P. Zhang, T. S. Safi, J. T. Hou, A. J.  
572 Grutter, and L. Liu, *Resonant Spin Transmission Mediated by Magnons in a Magnetic*  
573 *Insulator Multilayer Structure*, *Advanced Materials* **33**, 2008555 (2021).
- 574 [28] J. Olamit, K. Liu, Z.-P. Li, and I. K. Schuller, *Irreversibility of Magnetization Rotation in*  
575 *Exchange Biased Fe/Epitaxial-FeF<sub>2</sub> Thin Films*, *Appl Phys Lett* **90**, 032510 (2007).
- 576 [29] J. E. Davies, O. Hellwig, E. E. Fullerton, J. S. Jiang, S. D. Bader, G. T. Zimányi, and K. Liu,  
577 *Anisotropy Dependence of Irreversible Switching in Fe/SmCo and FeNi/FePt Exchange*  
578 *Spring Magnet Films*, *Appl Phys Lett* **86**, 262503 (2005).
- 579 [30] Yu. N. Khaydukov, D. Lenk, V. Zdravkov, R. Morari, T. Keller, A. S. Sidorenko, L. R. Tagirov,  
580 R. Tidecks, S. Horn, and B. Keimer, *Chirality of Bloch Domain Walls in Exchange-Biased*  
581 *CoO/Co Bilayer Studied by Waveguide-Enhanced Neutron Spin-Flip Scattering*, *Phys Rev B*  
582 **104**, 174445 (2021).
- 583 [31] H. Zhang, P. D. Gallagher, S. K. Satija, R. M. Lindstrom, R. L. Paul, T. P. Russell, P. Lambooy,  
584 and E. J. Kramer, *Grazing Incidence Prompt Gamma Emissions and Resonance-Enhanced*  
585 *Neutron Standing Waves in a Thin Film*, *Phys Rev Lett* **72**, 3044 (1994).
- 586 [32] T. Saerbeck, H. Huckfeldt, B. P. Toperverg, and A. Ehresmann, *Magnetic Structure of Ion-*  
587 *Beam Imprinted Stripe Domains Determined by Neutron Scattering*, *Nanomaterials* **10**, 752  
588 (2020).
- 589 [33] F. Radu, V. Leiner, K. Westerholt, H. Zabel, J. McCord, A. Vorobiev, J. Major, D. Jullien, H.  
590 Humblot, and F. Tasset, *Magnetic Induction and Domain Walls in Magnetic Thin Films at*  
591 *Remanence*, *Journal of Physics: Condensed Matter* **17**, 1711 (2005).
- 592 [34] E. Kentzinger, U. Rücker, B. Toperverg, F. Ott, and T. Brückel, *Depth-Resolved Investigation*  
593 *of the Lateral Magnetic Correlations in a Gradient Nanocrystalline Multilayer*, *Phys Rev B*  
594 **77**, 104435 (2008).
- 595 [35] S. P. Pogossian, A. Menelle, H. le Gall, J. M. Desvignes, and M. Artinian, *Experimental*  
596 *Observation of Guided Polarized Neutrons in Magnetic-Thin-Film Waveguides*, *Phys Rev B*  
597 **53**, 14359 (1996).
- 598 [36] S. v. Kozhevnikov, F. Ott, A. Paul, and L. Rosta, *Resonances and Off-Specular Scattering in*  
599 *Neutron Waveguides*, *Eur Phys J Spec Top* **167**, 87 (2009).
- 600 [37] Yu. Khaydukov, A. M. Petrzhik, I. v. Borisenko, A. Kalabukhov, D. Winkler, T. Keller, G. A.  
601 Ovsyannikov, and B. Keimer, *Magnetic Waveguides for Neutron Reflectometry*, *Phys Rev B*  
602 **96**, 165414 (2017).
- 603 [38] J. Olamit and K. Liu, *Rotational Hysteresis of the Exchange Anisotropy Direction in*  
604 *Co/FeMn Thin Films*, *J Appl Phys* **101**, 09E508 (2007).

- 605 [39] M. Z. Xue, S. L. Ding, R. Wu, L. Zha, G. Y. Qiao, H. L. Du, J. Z. Han, Y. C. Yang, C. S. Wang,  
606 and J. B. Yang, *Thickness Induced Uniaxial Anisotropy and Unexpected Four-Fold Symmetry*  
607 *in Co/SiO<sub>2</sub>/Si Films*, AIP Adv **8**, 056311 (2018).
- 608 [40] T. Kuschel, T. Becker, D. Bruns, M. Suendorf, F. Bertram, P. Fumagalli, and J. Wollschläger,  
609 *Uniaxial Magnetic Anisotropy for Thin Co Films on Glass Studied by Magneto-optic Kerr*  
610 *Effect*, J Appl Phys **109**, 093907 (2011).
- 611 [41] D. A. Gilbert, J. Olamit, R. K. Dumas, B. J. Kirby, A. J. Grutter, B. B. Maranville, E. Arenholz,  
612 J. A. Borchers, and K. Liu, *Controllable Positive Exchange Bias via Redox-Driven Oxygen*  
613 *Migration*, Nat Commun **7**, 11050 (2016).
- 614 [42] D. A. Gilbert, P. D. Murray, J. de Rojas, R. K. Dumas, J. E. Davies, and K. Liu, *Reconstructing*  
615 *Phase-Resolved Hysteresis Loops from First-Order Reversal Curves*, Sci Rep **11**, 4018  
616 (2021).
- 617 [43] E. B. Park, S.-U. Jang, J.-H. Kim, and S.-J. Kwon, *Induced Magnetic Anisotropy and Strain in*  
618 *Permalloy Films Deposited under Magnetic Field*, Thin Solid Films **520**, 5981 (2012).
- 619 [44] J. Trastoy, A. Camjayi, J. del Valle, Y. Kalcheim, J.-P. Crocombette, D. A. Gilbert, J. A.  
620 Borchers, J. E. Villegas, D. Ravelosona, M. J. Rozenberg, and I. K. Schuller, *Magnetic Field*  
621 *Frustration of the Metal-Insulator Transition in V<sub>2</sub>O<sub>3</sub>*, Phys Rev B **101**, 245109 (2020).
- 622 [45] H. J. Lauter, V. Lauter-Pasyuk, B. P. Toperverg, L. Romashev, V. Ustinov, E. Kravtsov, A.  
623 Vorobiev, O. Nikonov, and J. Major, *Spin-Resolved Unpolarized Neutron off-Specular*  
624 *Scattering for Magnetic Multilayer Studies*, Appl Phys A Mater Sci Process **74**, s1557  
625 (2002).
- 626 [46] T. J. Regan, H. Ohldag, C. Stamm, F. Nolting, J. Lüning, J. Stöhr, and R. L. White, *Chemical*  
627 *Effects at Metal/Oxide Interfaces Studied by x-Ray-Absorption Spectroscopy*, Phys Rev B  
628 **64**, 214422 (2001).
- 629 [47] J. F. K. Cooper, C. J. Kinane, S. Langridge, M. Ali, B. J. Hickey, T. Niizeki, K. Uchida, E. Saitoh,  
630 H. Ambaye, and A. Glavic, *Unexpected Structural and Magnetic Depth Dependence of YIG*  
631 *Thin Films*, Phys Rev B **96**, 104404 (2017).
- 632 [48] S. Pütter, S. Geprägs, R. Schlitz, M. Althammer, A. Erb, R. Gross, and S. T. B. Goennenwein,  
633 *Impact of the Interface Quality of Pt/YIG(111) Hybrids on Their Spin Hall*  
634 *Magnetoresistance*, Appl Phys Lett **110**, 012403 (2017).
- 635 [49] Q. Shao, A. Grutter, Y. Liu, G. Yu, C.-Y. Yang, D. A. Gilbert, E. Arenholz, P. Shafer, X. Che, C.  
636 Tang, M. Aldosary, A. Navabi, Q. L. He, B. J. Kirby, J. Shi, and K. L. Wang, *Exploring*  
637 *Interfacial Exchange Coupling and Sublattice Effect in Heavy Metal/Ferrimagnetic*  
638 *Insulator Heterostructures Using Hall Measurements, x-Ray Magnetic Circular Dichroism,*  
639 *and Neutron Reflectometry*, Phys Rev B **99**, 104401 (2019).
- 640
- 641